SUZAKU VIEW OF THE *SWIFT*/BAT ACTIVE GALACTIC NUCLEI. III. APPLICATION OF NUMERICAL
TORUS MODELS TO TWO NEARLY COMPTON THICK AGNS (NGC 612 AND NGC 3081)

Satoshi Eguchi[1], Yoshihiro Ueda[1], Hisamitsu Awaki[2], James Aird[3], Yuichi Terashima[2], and Richard Mushotzky[4]

ABSTRACT

The broad band spectra of two *Swift*/BAT AGNs obtained from *Suzaku* follow-up observations are studied: NGC 612 and NGC 3081. Fitting with standard models, we find that both sources show similar spectra characterized by a heavy absorption with $N_{\rm H} \simeq 10^{24}$ cm^{-2}, the fraction of scattered light is $f_{\rm scat} = 0.5 - 0.8\%$, and the solid angle of the reflection component is $\Omega/2\pi = 0.4 - 1.1$. To investigate the geometry of the torus, we apply numerical spectral models utilizing Monte Carlo simulations by Ikeda et al. (2009) to the *Suzaku* spectra. We find our data are well explained by this torus model, which has four geometrical parameters. The fit results suggest that NGC 612 has the torus half opening-angle of $\simeq 60° - 70°$ and is observed from a nearly edge-on angle with a small amount of scattering gas, while NGC 3081 has a very small opening angle $\simeq 15°$ and is observed on a face-on geometry, more like the deeply buried "new type" AGNs found by Ueda et al. (2007). We demonstrate the potential power of direct application of such numerical simulations to the high quality broad band spectra to unveil the inner structure of AGNs.

Subject headings: galaxies: active — gamma rays: observations — X-rays: galaxies — X-rays: general

1. INTRODUCTION

The strong correlation between the mass of a supermassive black hole (SMBH) and that of the galactic bulge (e.g., Magorrian et al. 1998; Marconi & Hunt 2003) suggests a fundamental link between the growth of SMBH and galaxy evolution. Theoretical models predict that most SMBHs in galaxies experience a heavily obscured phase in their growth stage (e.g., Hopkins et al. 2005). Indeed, studies based on population synthesis models of the cosmic X-ray background (CXB) suggest that heavily obscured AGNs, whose line-of-sight hydrogen column density ($N_{\rm H}$) is greater than $10^{23.5}$ cm^{-2}, are a significant fraction of the AGN population (Ueda et al. 2003; Gilli et al. 2007). Due to the difficulty of detecting them in most energy bands, however, our understanding of heavily obscured AGNs (including "Compton-thick" ones with $N_{\rm H} > 10^{24}$ cm^{-2}) is very scarce even in the local universe.

Sensitive hard X-ray observations above 10 keV, where the penetrating power overwhelms photo-electric absorption, provide fruitful information about this population, except for heavily Compton thick ($N_{\rm H} \gtrsim 10^{24.5}$ cm^{-2}) objects. Recent all sky hard X-ray surveys performed with *Swift*/BAT (15–200 keV; Tueller et al. 2008) and *INTEGRAL* (10–100 keV; Bassani et al. 2006; Krivonos et al. 2007) are ideal for this purpose with much less selection biases than surveys at lower energies. Our team have been working on a systematic follow-up

observation program with *Suzaku* of Swift/BAT detected AGNs whose broad band X-ray spectra were poorly (or never) studied previously, targeting obscured objects in most cases. Ueda et al. (2007) discovered deeply buried AGNs that exhibit very small fractions of scattered soft X-rays ($< 0.5\%$) with respect to the transmitted component, with strong reflection signals most probably coming from the inner wall of the Compton-thick tori. Further studies of six Swift AGNs by Eguchi et al. (2009) (Paper I hereafter) show that they could be classified into two types, "new type" AGNs with a small scattering fraction and strong reflection strength, and "classical type" ones with a larger scattering fraction and weaker reflection. These types are consistent with SMBHs surrounded by geometrically thick and thin tori, respectively. Using an *INTEGRAL* selected sample, Comastri et al. (2009) also suggest that there are distinct AGN populations of new and classical types, although the result depends on whether the absorption for the reflection component is considered or not in the spectral model (see Comastri et al. 2010). Due to the limited number of objects in the sample studied we are far from reaching a consensus on the torus structure and its dependence on various parameters like the AGN luminosity, Eddington ratio, and properties of the host-galaxy, for the whole AGN populations.

High quality broad band X-ray spectra give unique insight into the structure and geometry of the central region of AGNs. Most previous studies, however, relied on phenomenological spectral models where the detailed geometry of the torus is not taken into account; usually, an analytical formula for the Compton reflection from matter with infinite optical depths is simply assumed for the reprocessed emission, and absorption column density of the transmitted component is treated independently. Monte Carlo simulation is a powerful tool to reproduce realistic spectra from AGNs with a com-

[1] Department of Astronomy, Kyoto University, Kyoto 606-8502, Japan
[2] Department of Physics, Faculty of Science, Ehime University, Matsuyama 790-8577, Japan
[3] Center for Astrophysics and Space Sciences (CASS), Department of Physics, University of California, San Diego, CA 92093, USA
[4] Department of Astronomy, University of Maryland, College Park, MD, USA

Table 1
List of Targets

SWIFT	Optical/IR Identification	R.A. (J2000)	Dec. (J2000)	Redshift	Classification
J0134.1–3625	NGC 612	01 33 57.74	-36 29 35.7	0.0298	Seyfert 2
J0959.5–2258	NGC 3081	09 59 29.54	-22 49 34.6	0.0080	Seyfert 2

Note. — The position, redshift, and classification for each source is taken from the NASA/IPAC Extragalactic Database.

plex structure of the torus, which may not always have a sufficiently large optical depth for Compton scattering. Recently, Ikeda et al. (2009) have developed such a Monte Carlo code that can be applicable to the broad band X-ray spectra with several free parameters describing the torus geometry. Similarly, Murphy & Yaqoob (2009) also studied the numerical spectra from a toroidal torus, known as the MYTORUS model[5], although we do not adopt this model here because the opening angle of the torus is fixed at 60°. Applying such models directly to the observed spectra, we can obtain more accurate constraints on the inner structure of AGNs than from the standard previous analysis.

In this paper, we present the results of detailed X-ray spectral analysis of *Suzaku* data of two *Swift*/BAT AGNs, Swift J0134.1–3625 (NGC 612; $z = 0.0298$) and Swift J0959.5–2258 (NGC 3081; $z = 0.0080$), whose simultaneous broad band spectra were not available before. NGC 612 is a powerful radio galaxy, which was originally classified as Fanaroff-Riley (FR; Fanaroff & Riley 1974) II type by Morganti et al. (1993). This object hosts prominent double radio sources; the eastern lobe has a bright hot spot near its outer edge, while the western one has a jet-like structure. Since the former and latter morphology correspond to those of the FR I and II types, respectively, Gopal-Krishna & Wiita (2000) classifies it as a hybrid morphology radio source. NGC 612 shows an optical spectrum of Seyfert 2 galaxies but the intensity of the [O III] emission is very weak (Parisi et al. 2009). Winter et al. (2008) present the X-ray spectrum observed with *XMM-Newton*, obtaining a large hydrogen column density of $N_H \simeq 10^{23.9}$ cm^{-2} with an apparently very flat power-law index of $\simeq 0.3$, suggestive of a reflection-dominant spectrum below 10 keV. NGC 3081 is a Seyfert 2 hosted by a barred galaxy. This object has three rings associated with a tidal interaction (Freeman et al. 2000), and exhibits time variable polarization in the optical band (Joshi et al. 1989). The strong [O III] emission is observed from this object (Storchi-Bergmann et al. 1995). Moran et al. (2001) report a large absorption column density ($N_H \simeq 10^{23.7}$ cm^{-2}) from the X-ray spectrum observed with *ASCA*.

Section 2 describes the observations and data reduction of the two sources. We first analyze the spectra with standard spectral models in Section 3, and then present the results of application of the torus model utilizing Monte Carlo calculation by Ikeda et al. (2009) in Section 4. The implications of our results are discussed in Section 5. We adopt the cosmological parameters (H_0, Ω_m, Ω_λ) = (70 km s^{-1} Mpc^{-1}, 0.3, 0.7) throughout the paper.

2. OBSERVATION AND DATA REDUCTION

2.1. *Observation*

We observed NGC 612 and NGC 3081 with *Suzaku* in 2008 May and June, respectively. The basic information for our targets is summarized in Table 1. *Suzaku* (Mitsuda et al. 2007) carries four X-ray CCD cameras called the X-ray Imaging Spectrometer (XIS-0, XIS-1, XIS-2, and XIS-3) as focal plane imager of four X-ray telescopes, and a non-imaging instrument called the Hard X-ray Detector (HXD) consisting of Si PIN photo-diodes and GSO scintillation counters. XIS-0, XIS-2, and XIS-3 are front-side illuminated CCDs (FI-XISs), while XIS-1 is the back-side illuminated one (BI-XIS). To maximize the effective area of the HXD, the targets were observed at the HXD nominal position, which is about 5 arcmin off-axis from the averaged optical axis of the XISs.[6]

We analyze only the data of the XISs and the HXD/PIN, which covers the energy band of 0.2–12 keV and 10–60 keV, respectively. The fluxes above 50 keV are too faint to be detected with HXD/GSO. Table 2 shows the log of the observations. The net exposure of each target is about 45 ks. Because XIS-2 became unoperatable on 2007 November 7 (Dotani et al. 2007), no XIS-2 data are available for both objects. For the XIS observations, we applied spaced-row charge injection (SCI) to improve the energy resolution (Nakajima et al. 2008); for instance, it reduces the full width at half maximum of the ^{55}Fe calibration source from $\simeq 230$ eV to $\simeq 160$ eV for XIS-0 (Ozawa et al. 2009). To constrain the broad band spectra above 60 keV, we also utilize the *Swift*/BAT spectra covering the 15–200 keV band, integrated over the first 22-months of *Swift* operations.
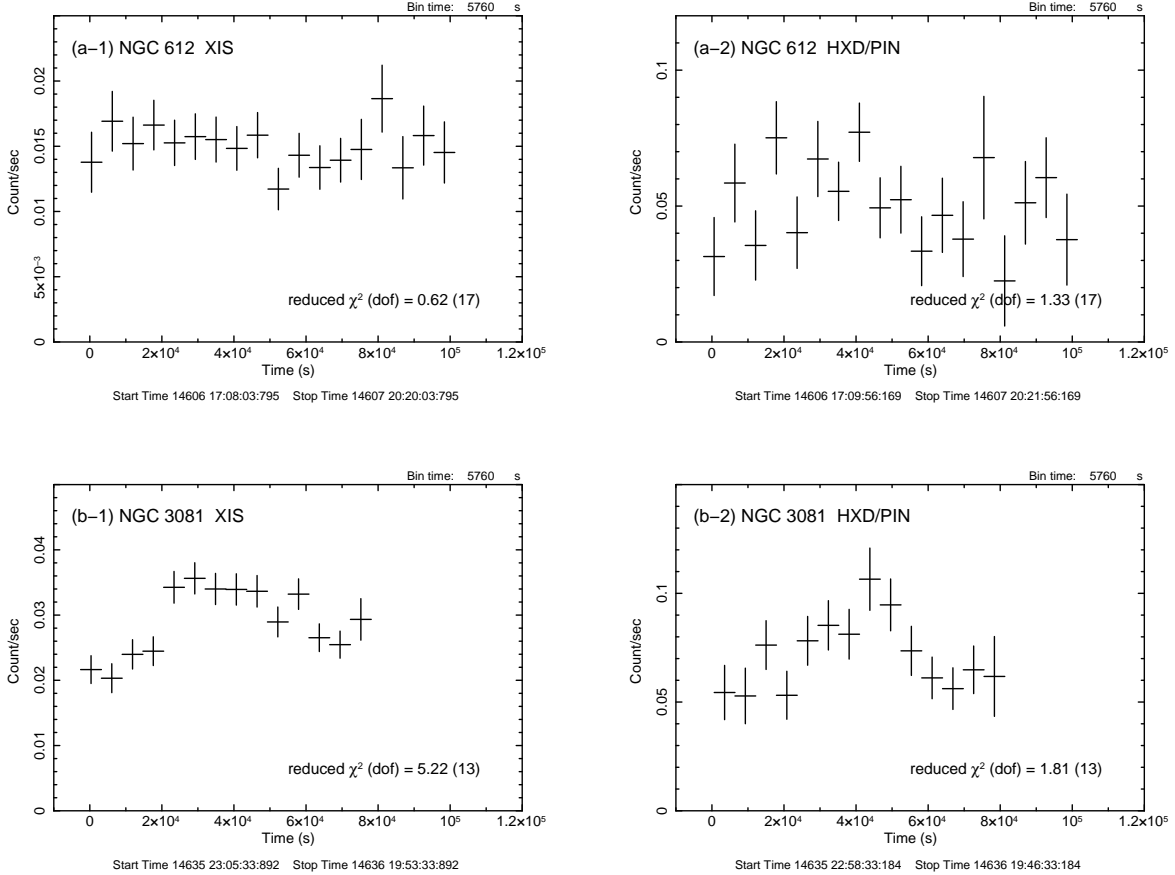
2.2. *Data Reduction*

The *Suzaku* data are analyzed by using *HEAsoft* version 6.7 and the latest version of *CALDB* on 2009 December 3. For the XIS data, we analyze the version 2.2 cleaned events distributed by the *Suzaku* pipeline processing team. In extraction of the light curves and spectra, we set the source region as a circle around the detected position with a radius of 1.5 arcmin, where about 75% of the total source photons are accumulated, to maximize the signal-to-noise ratio. The background for the XIS data is taken from a source-free region in the field of view with an approximately same offset angle from the optical axis as the source. For the non X-ray background of the HXD/PIN data, we use the so-called "tuned" background model provided by the HXD team. Its systematic errors are estimated to be $\simeq 0.97\%$ at a 1σ confidence level in the 15–40 keV band for a 40 ks exposure

---

[5] http://www.mytorus.com/

[6] http://heasarc.gsfc.nasa.gov/docs/suzaku/analysis/abc/

Table 2
Observation Log

Target	Start Time (UT)	End Time	Exposure[a] (XIS)	Exposure (HXD/PIN)	SCI[b]
NGC 612	2008 May 20 16:19	May 21 20:08	48.5 ks	41.3 ks	On
NGC 3081	2008 Jun 18 21:49	Jun 19 19:33	43.7 ks	42.4 ks	On

[a] Based on the good time interval for XIS-0.
[b] With/without the spaced-row charge injection for the XIS (Nakajima et al. 2008).

Figure 1. The background subtracted light curves of *Suzaku*. One bin corresponds to 96 minutes. The numbers listed in each panel represent the value of reduced χ^2 with the degrees of freedom for the constant flux hypothesis. *Left*: The light curves of the XIS in the 2–10 keV band. The data from the XIS-0 and XIS-3 are summed. *Right*: The light curves of the HXD/PIN in the 15–40 keV band.

(Mizuno et al. 2008). Since our exposures are ≈ 40 ks or longer, we expect that the error is even smaller than this value. The CXB spectrum simulated with the HXD/PIN response for a uniformly extended emission is added to the non X-ray background spectrum.

2.3. *Light Curves*

Figure 1 shows the background-subtracted light curves of our targets obtained with the XIS and HXD/PIN in the 2–10 keV and 15–40 keV bands, respectively. To minimize any systematic uncertainties caused by the orbital change of satellite, we merge data taken during one orbit ($\simeq 96$ minutes) into one bin. Then, to check if there are any significant time variability during the observations, we perform a simple χ^2 test to each light curve assuming a null hypothesis of a constant flux. The resultant reduced χ^2 value and the degrees of freedom are shown in each panel. As noticed from Figure 1, the 2–10 keV flux of NGC 3081 increased by a factor of 1.5 af-

ter $\simeq 20$ ks from the start of the observation. Then, a flux decline is suggested between $\simeq 50$ ks and $\simeq 60$ ks particularly in the 15–40 keV band. Thus, we divide the observation of NGC 3081 into three different time regions, 0–20 ks (Epoch 1), 20–60 ks (Epoch 2), and 60–80 ks (Epoch 3) measured from the observation start. By contrast, no significant time variability on a time scale of hours are detected from NGC 612. Hence, we analyze the time-averaged spectra over the whole observation for NGC 612.

2.4. *BAT Spectra*

It is known that the incident photon spectra of Seyfert galaxies are roughly approximated by a power law with an exponential cutoff (cutoff power-law model), represented as $AE^{-\Gamma}\exp(-E/E_{\rm cut})$, where A, Γ, $E_{\rm cut}$ are the normalization at 1 keV, photon index, and cutoff energy, respectively. We analyze the *Swift*/BAT spec-

Table 3
Cutoff Energies (E_{cut}) determined
by the BAT spectra

$\Omega/2\pi$	NGC 612	NGC 3081
0	> 315	> 338
χ^2/d.o.f.	16.4/6	11.6/6
2	> 319	> 293
χ^2/d.o.f.	10.3/6	5.8/6

Note. — The unit of E_{cut} is keV.

tra in the 15–200 keV band to constrain E_{cut}. Here we take into account possible contribution from a Compton reflection component from optically thick, cold matter, utilizing the **pexrav** code Magdziarz & Zdziarski (1995). The relative intensity of the reflection component to that of the intrinsic cutoff power-law component is defined as $R \equiv \Omega/2\pi$, where Ω is the solid angle of the reflector ($R = 1$ corresponds to the reflection from a semi-infinite plane).

In the analysis of the *Swift*/BAT spectra, we assume $R = 0$ or 2 as the two extreme cases just to evaluate the effects of including the reflection components, as done in Paper I. The inclination angle is fixed at 60°. To avoid strong coupling between the power-law slope and cutoff energy, we fix the photon index at 1.9, the canonical slope for AGNs (e.g., Nandra & Pounds 1994). Table 3 gives the fitting results for E_{cut}; we find that E_{cut} is greater than $\simeq 300$ keV for both targets.[7] Accordingly, we fix it at 300 keV (or 360 keV for consistency with the Ikeda model) in the following spectral analysis.

3. ANALYTICAL MODELS

We perform the spectral fitting to the *Suzaku* data in the same manner as Paper I. We start with the simplest model for each target, and if we find that the fit with a simple model does not give a physically self-consistent picture or that the fit is significantly improved by introducing additional parameters, then we adopt more complicated models. We use only the *Suzaku* XIS and HXD/PIN data throughout this stage, and finally perform the simultaneous fit of XIS, HXD/PIN, and *Swift*/BAT spectra with the selected model to obtain the best-fit parameters.

The spectra of FI-XISs are summed, and the relative normalization between the FI-XISs and the PIN is fixed at 1.18 based on the calibration of Crab Nebula (Maeda et al. 2008). Those of BI-XIS and BAT against FI-XISs are set as free parameters. The Galactic absorption (N_H^{Gal}) is always included in the models, whose hydrogen column density is fixed at values obtained from the H I map Kalberla et al. (2005), available with the **nh** program in the *HEAsoft* package. We adopt the photoelectric absorption cross section by Balucinska-Church & McCammon (1992) ("bcmc"). Different from Paper I, we allow the iron abundance to be a free parameter by using **zvphabs** because non Solar values (as defined by Anders & Grevesse 1989) are required to explain the *Suzaku* spectra, while Solar abun-
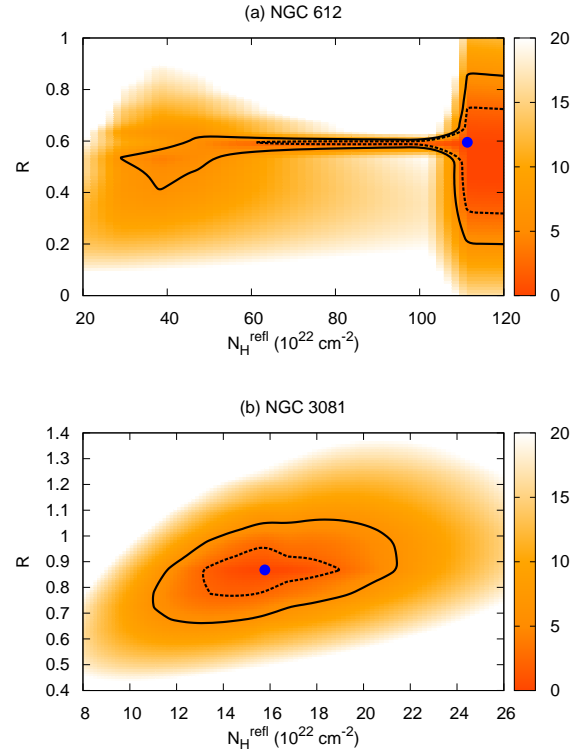

Figure 2. The confidence map in $\Delta\chi^2$ (color scale) with respect to the strength of the reflection component ($R = \Omega/2\pi$) and its absorption (N_H^{refl}) for NGC 612 (top) and NGC 3081 (bottom). The dashed and solid curves correspond to the 1σ and 2σ confidence level for two interesting parameters, respectively.

dances are adopted for the other metals throughout our analysis.

We use the same three models as defined in Paper I, consisting of an absorbed transmitted component, a scattered component, and/or an absorbed reflection component, with an iron-K emission line:

- Model A: transmission + scattering + iron line,[8]

- Model B: transmission + scattering + iron line + absorbed reflection,[9]

- Model C: transmission with dual absorber + scattering + iron line + absorbed reflection.[10]

In our analysis, we adopt an unabsorbed power law with the same photon index as the incident continuum to describe the scattered component, ignoring any emission lines from the photo-ionized gas. Note that here we only introduce a single absorber for the reflection component as the simplest approximation, although we expect both absorbed and unabsorbed ones from the torus as well as that from the accretion disk, as described in next Section. The **pexrav** component in each spectral model (see footnote) represents only the reflection component not including the direct one by setting $R < 0$, and the

---

[7] This conclusion is unchanged when we fix the inclination angle at 30° or 80°, indicating that E_{cut} is not sensitive to the assumed inclination angle.

[8] In *XSPEC* nomenclature, **zvphabs*zhighect*zpowerlw + const*zhighect*zpowerlw + zgauss**

[9] In *XSPEC* nomenclature, **vzphabs*zhighect*zpowerlw + const*zhighect*zpowerlw + zgauss + zvphabs*pexrav**

[10] In *XSPEC* nomenclature, **zvphabs*zpcfabs*zhighect*zpowerlw + const*zhighect*zpowerlw + zgauss + zvphabs*pexrav**

inclination angle is fixed at $60°$. Theoretically, the equivalent width (E.W.) of the iron-K emission line with respect to the reflection component, E.W.$^{\text{refl}}$, is expected to be ~ 1 keV (Matt et al. 1991). Since this value depends on the geometry of the reflector as well as the iron abundance, we regard the result as physically valid if E.W.$^{\text{refl}} = 0.5$–2 keV. No other emission lines than iron $K\alpha$ are significantly detected from the spectra. Considering calibration uncertainties in the energy response of the XISs, we fix the 1σ line width of the iron-$K\alpha$ emission at the averaged value of the (apparent) line width of the ^{55}Fe calibration source at 5.9 keV: 45 eV and 47 eV for NGC 612 and NGC 3081, respectively.

3.1. *NGC 612*

Model B is adopted as the most appropriate model of NGC 612. We obtain $(\chi^2, \nu) = (90.8, 85)$ with Model A and $(\chi^2, \nu) = (86.9, 84)$ with Model B from the *Suzaku* spectra, where ν is the degree of freedom. Thus, the improvement of the fit by adding a reflection component is found to be significant at 94% confidence level by an F-test. No significant improvement is found with Model C. For this target, the absorption to the reflection component $N_{\text{H}}^{\text{refl}}$ is linked to that for the transmitted component, because making them independent does not give a better fit over the statistics (see below). Since the E.W. of the iron-K line with respect to the reflection component is E.W.$^{\text{refl}} = 0.7 \pm 0.1$ keV, the model is physically self-consistent; the iron abundance of NGC 612 is roughly half of the Solar value, $0.54^{+0.10}_{-0.07}$, obtained from the simultaneous fit of the *Suzaku* and BAT spectra.

To examine the degeneracy in the fitting parameters, in Figure 2 (top) we show the confidence map (in terms of $\Delta\chi^2$) with respect to the strength of the reflection component (R) and its absorption ($N_{\text{H}}^{\text{refl}}$), based on the Model B fit including the BAT data. Here we do not link $N_{\text{H}}^{\text{refl}}$ to that of the transmitted component (N_{H}), and explore a region of $N_{\text{H}}^{\text{refl}} < 1.2 \times 10^{24}$ cm^{-2}, the upper limit obtained for N_{H}. The contours give the confidence levels at 1σ and 2σ for two interesting parameters. As noticed, while a wide range of $N_{\text{H}}^{\text{refl}}$ ($\gtrsim 6 \times 10^{23}$ cm^{-2}, 1σ) is allowed, we can constrain the reflection strength to be $R \simeq 0.6$ for $N_{\text{H}}^{\text{refl}} < 1.1 \times 10^{24}$ cm^{-2} and $R \simeq 0.3 - 0.7$ otherwise. The case of an unabsorbed reflection component ($N_{\text{H}}^{\text{refl}} = 0$) or no reflection component ($R = 0$) is rejected at $> 99\%$ confidence level, which corresponds to $\Delta\chi^2 = 9.21$.

3.2. *NGC 3081*

First, we analyze the *Suzaku* spectra integrated over Epoch 1. We obtain $(\chi^2, \nu) = (120.1, 61)$ with Model A and $(\chi^2, \nu) = (80.2, 59)$ with Model B, and thus the improvement of χ^2 is significant at $> 99\%$ confidence level by an F-test. No significant improvement is found with Model C. Finally, since positive residuals remain in the energy band below 1 keV, we add the **vapec**[11] in *XSPEC*, a spectral model from an optically-thin thermal plasma, whose iron abundance is linked to that in the absorber of the transmitted component. This yields a further significantly better fit at $> 99\%$ confidence level

[11] http://cxc.harvard.edu/atomdb/

with $(\chi^2, \nu) = (50.7, 57)$. The E.W. of the iron-K line with respect to the reflection component is E.W.$^{\text{refl}} = 1.5 \pm 0.3$ keV, which is self-consistent. Thus, we adopt Model B+**vapec** as the best fit model for Epoch 1.

By fitting the Epoch 2 and 3 spectra of *Suzaku* with the same model, we obtain acceptable fits with $(\chi^2, \nu) = (139.7, 114)$ and $(19.1, 30)$, respectively. The best-fit parameters in the three epochs are plotted in Figure 3 except for the iron abundance and those of the thin thermal component, which are expected to show no time variability. We find only a weak indication that the column density changed during the observation from $N_{\text{H}} = (113 \pm 10) \times 10^{22}$ cm^{-2} (Epoch 1), to $N_{\text{H}} = (98 \pm 6) \times 10^{22}$ cm^{-2} (Epoch 2), and then $N_{\text{H}} = (86 \pm 10) \times 10^{22}$ cm^{-2} (Epoch 3) in addition to the unabsorbed power-law luminosity, which varied from $L_{2-10} = (3.0 \pm 0.2) \times 10^{42}$ ergs s^{-1} (Epoch 1), to $L_{2-10} = 3.8^{+0.2}_{-0.3} \times 10^{42}$ ergs s^{-1} (Epoch 2), and $L_{2-10} = 2.7^{+0.5}_{-0.2} \times 10^{42}$ ergs s^{-1} (Epoch 3) in the 2–10 keV band. The other parameters are found to be consistent with being constant among the three epochs within the errors. The significance of the variability of the column density is marginal, as the null hypothesis probability of a constant value is found to be 15% from a χ^2 test. Thus, we sum the Epoch 1, 2 and 3 data of *Suzaku* and discuss the time averaged spectra in the following analysis.

To best constrain the spectral parameters of NGC 3081, we perform the simultaneous fit to the time-averaged *Suzaku* and BAT spectra with the Model B+**vapec** model. This yields $(\chi^2, \nu) = 0(199.28, 199)$ and E.W.$^{\text{refl}} = 1.0 \pm 0.1$ keV, and thus is physically self-consistent. The iron abundance with respect to Solar is 0.89 ± 0.07, and the temperature of the plasma is found to be $kT = 0.26 \pm 0.02$ keV with an emission measure of $n^2V \simeq 1.5 \times 10^{63}$ cm^{-3}.

Figure 2 (bottom) shows the confidence contour map with respect to R and $N_{\text{H}}^{\text{refl}}$ based on Model B (including the BAT data) for NGC 3081. Unlike the case of NGC 612, the solution is well constrained ($R \simeq 0.8 - 1.0$, 1σ) and we do not see strong degeneracy in the fitting parameters. Again, neither the case of an unabsorbed reflection component ($N_{\text{H}}^{\text{refl}} = 0$), nor no reflection component ($R = 0$) is allowed at $> 99\%$ confidence level.

3.3. *Results Summary of Analytical Models*

We summarize the best-fit models and parameters in Table 4. The observed fluxes in the 2–10 keV and 10–50 keV bands, and the estimated 2–10 keV intrinsic luminosities corrected for absorption are also listed. Figure 4 (left) shows the observed spectra of the FI-XIS (black), the BI-XIS (red), and the HXD/PIN (magenta) folded with the detector response in units of counts s^{-1} keV^{-1}, together with the *unfolded* BAT spectra (blue) in units of photons cm^{-2} ks^{-1} keV^{-1}. The best-fit models are superposed by solid lines. In the lower panels, the corresponding data-to-model residuals in units of χ (i.e., normalized by the 1σ statistical error in each bin) are plotted. Figure 4 (right) shows the best-fit spectral models in units of EF_E without Galactic absorption, where the contribution of each component is plotted separately; the black, red, blue, cyan, magenta curves correspond to the total, transmitted component, reflection component,
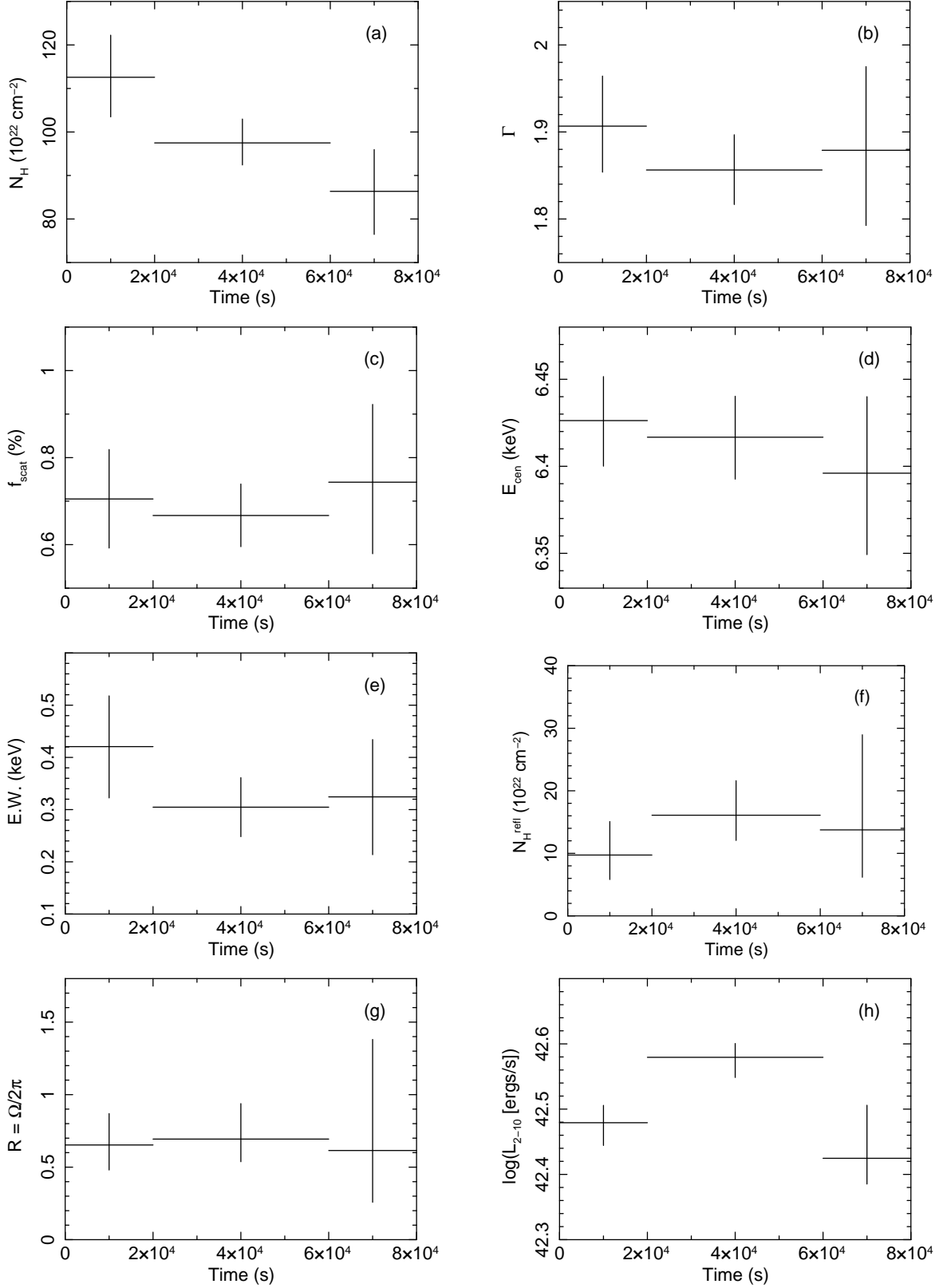
Figure 3. Time variability of the best-fit parameters of NGC 3081 obtained with the analytical model: from left to right and top to bottom, (a) the line-of-sight hydrogen column density for the transmitted component, (b) the power-law photon index, (c) the fraction of the scattered component relative to the intrinsic power law, (d) the center energy of the iron-K emission line at the rest frame, (e) the equivalent width of the iron-K line with respect to the whole continuum, (f) the line-of-sight hydrogen column density for the reflection component, (g) the solid angle of the reflection component, (h) the 2–10 keV intrinsic luminosity corrected for the absorption.
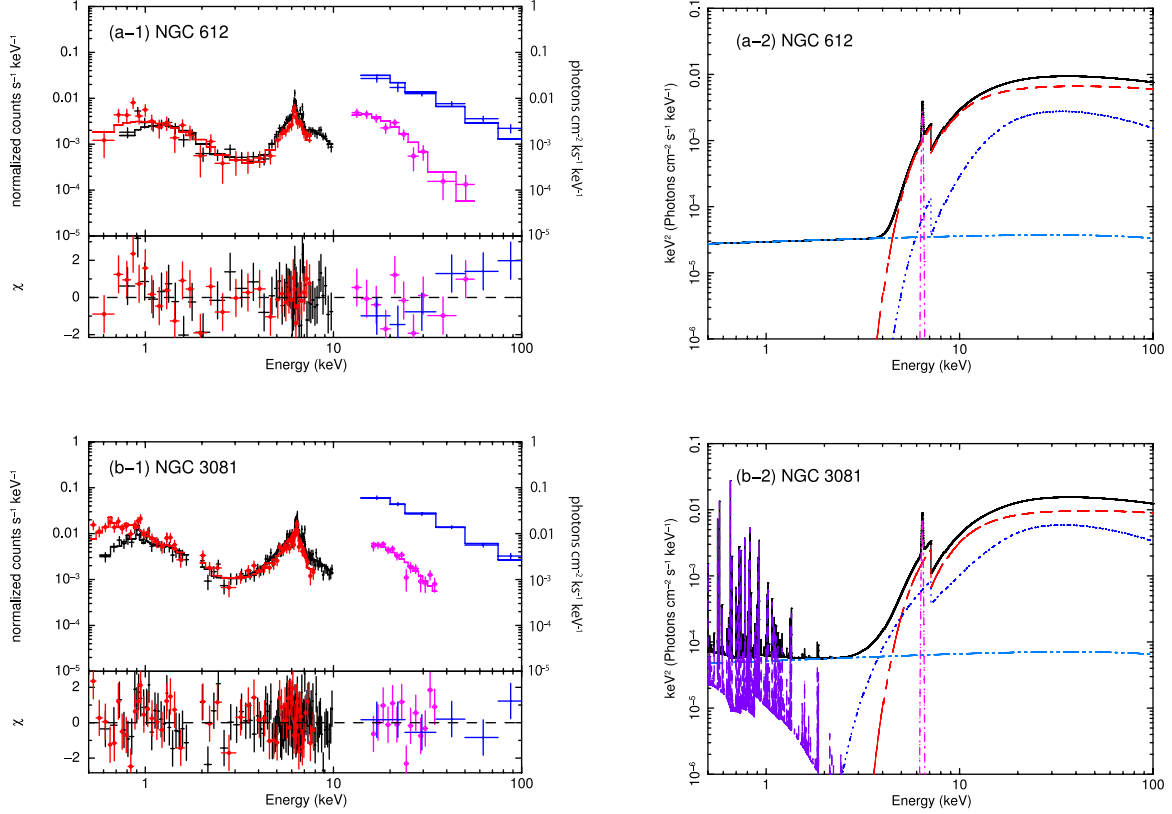
Figure 4. The observed spectra (left) and the best-fit spectra model (right) of NGC 612 and NGC 3081. *Left*: The black crosses, red filled circles, magenta open circles, and blue crosses represent the data of the FI-XIS, BI-XIS, HXD/PIN, and BAT, respectively, with 1σ error bars. The spectra of the XIS and PIN are folded with the detector responses in units of counts s^{-1} keV^{-1}, while those of the BAT are *unfolded* spectra in units of photons cm^{-2} ks^{-1} keV^{-1}. The best-fit models are plotted by solid curves, and the residuals in units of χ are shown in the lower panels. *Right*: The best-fit spectral model in units of EF_E (where E is the energy and F_E is the photon spectrum). The black, dashed red, dotted blue, dot-dot-dashed cyan, dot-dashed magenta curves correspond to the total, transmitted one, reflection component, scattered component, and iron-K emission line, respectively. The purple dashed model below 2 keV in NGC 3081 represents the emission from an optically-thin thermal plasma (see text).

Table 4
Best-fit Spectral Parameters with Analytical Models

		NGC 612	NGC 3081
	Best-fit model	B	B + vapec[a]
(1)	$N_{\rm H}^{\rm Gal}$ (10^{22} cm^{-2})	0.0195	0.0388
(2)	$N_{\rm H}$ (10^{22} cm^{-2})	111 ± 5	98 ± 4
(3)	$Z_{\rm Fe}$	$0.54^{+0.10}_{-0.07}$	0.89 ± 0.07
(4)	Γ	1.90 ± 0.04	1.88 ± 0.02
(5)	$f_{\rm scat}$ (%)	0.55 ± 0.06	0.73 ± 0.07
(6)	$E_{\rm cen}$ (keV)	$6.42^{+0.03}_{-0.02}$	6.41 ± 0.02
(7)	E.W. (keV)	0.28 ± 0.06	0.35 ± 0.05
(8)	E.W.$^{\rm refl}$ (keV)	0.7 ± 0.1	1.0 ± 0.1
(9)	$N_{\rm H}^{\rm refl}$ (10^{22} cm^{-2})	$(= N_{\rm H})$	16^{+4}_{-3}
(10)	R	0.6 ± 0.2	0.9 ± 0.2
(11)	F_{2-10} (ergs cm^{-2} s^{-1})	1.6×10^{-12}	2.7×10^{-12}
(12)	F_{10-50} (ergs cm^{-2} s^{-1})	1.9×10^{-11}	3.1×10^{-11}
(13)	L_{2-10} (ergs s^{-1})	3.0×10^{43}	3.0×10^{42}
	χ^2/d.o.f.	100.4/91	199.3/199

Note. — (1) The hydrogen column density of Galactic absorption by Kalberla et al. (2005). (2) The line-of-sight hydrogen column density for the transmitted component. (3) The iron abundance relative to the Solar value. (4) The power-law photon index. (5) The fraction of the scattered component relative to the intrinsic power law. (6) The center energy of the iron-K emission line at the rest frame of the source redshift. (7) The observed equivalent width of the iron-K line with respect to the whole continuum. (8) The observed equivalent width of the iron-K line with respect to the reflection component (9) The line-of-sight hydrogen column density for the reflection component. (10) The relative strength of the reflection component to the transmitted one, defined as $R \equiv \Omega/2\pi$, where Ω is the solid angle of the reflector viewed from the nucleus. (11) The observed flux in the 2–10 keV band. (12) The observed flux in the 10–50 keV band. (13) The 2–10 keV intrinsic luminosity corrected for the absorption. The errors are 90% confidence limits for a single parameter.
[a] An additional emission from an optically-thin thermal plasma is required, modelled by the **vapec** code with a temperature of $kT = 0.26 \pm 0.02$ keV and an emission measure of 1.5×10^{63} cm^{-3}. The iron abundance is linked to that in the absorber of the transmitted component (see text).

scattered component, and iron-K emission line, respectively. For NGC 3081, the additional soft component is also included in purple.

We find that the fraction of the scattered component with respect to the transmitted one for both of NGC 612 and NGC 3081 are fairly small (0.5%–0.8%). Also, they are heavily obscured with column densities of $N_{\rm H} \simeq 10^{24}$ cm^{-2}, and hence can be regarded as nearly "Compton thick" AGNs. Figure 5 shows the correlation between the reflection component R and the scattered component $f_{\rm scat}$, superposed on the same plot presented in Paper I. NGC 612 and NGC 3081 are located on a similar position to each other in this plot. In Paper I, the authors categorize the observed AGNs into two groups: "new type" with $R \gtrsim 0.8$ and $f_{\rm scat} \lesssim 0.5\%$, and "classical type" with $R \lesssim 0.8$ and $f_{\rm scat} \gtrsim 0.5\%$. Since our targets are placed just between the two types, it is not clear to which "type" these AGNs belong if the intrinsic distribution is indeed distinct. It is also possible that the distribution is smooth and they actually represent an intermediate class bridging the two types.

4. TORUS MODEL

Ikeda et al. (2009) performed a set of Monte Carlo simulations to calculate a realistic reprocessed emission from the torus irradiated by a central source, which is assumed

to be a cutoff power-law model. In the simulation, they assume a 3-dimensional axis-symmetric uniform torus as illustrated in Figure 6. It is characterized by the half-opening angle $\theta_{\rm oa}$, the inclination angle of torus from an observer $\theta_{\rm inc}$, the hydrogen column density viewed from the equatorial plane $N_{\rm H}^{\rm Eq}$, and the ratio r of $r_{\rm in}$ to $r_{\rm out}$.

4.1. Method

To perform spectral fitting on XSPEC with the Ikeda et al. (2009) model, we utilize an **atable** model where the resultant spectra from Monte Carlo calculation are stored at grids of the torus parameters in FITS files. Here we refer to the results of the continuum reprocessed from the torus ("torus-reflection component") and those of iron-K fluorescence line, assuming the geometry with $r \equiv r_{\rm in}/r_{\rm out} = 0.01$. The cutoff energy is fixed at $E_{\rm cut} = 360$ keV throughout our analysis, which is con-
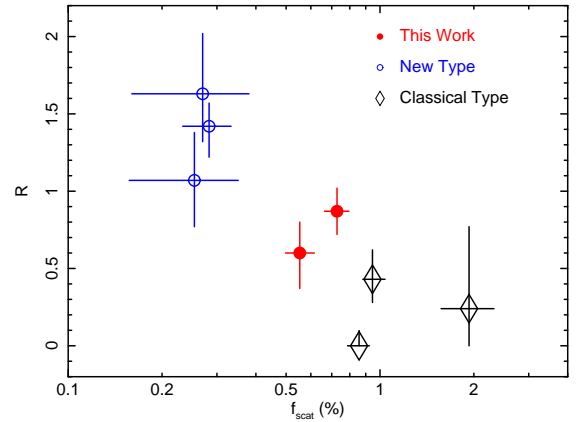

Figure 5. The correlation between the strength of the Compton reflection component ($R = \Omega/2\pi$) and the fraction of the scattered component ($f_{\rm scat}$) for our targets (filled circles), superposed on the same figure taken from Paper I, where open circle and open diamond represent "new type" ($R \gtrsim 0.8$ and $f_{\rm scat} \lesssim 0.5\%$) and "classical type" ($R \lesssim 0.8$ and $f_{\rm scat} \gtrsim 0.5\%$) AGNs, respectively.
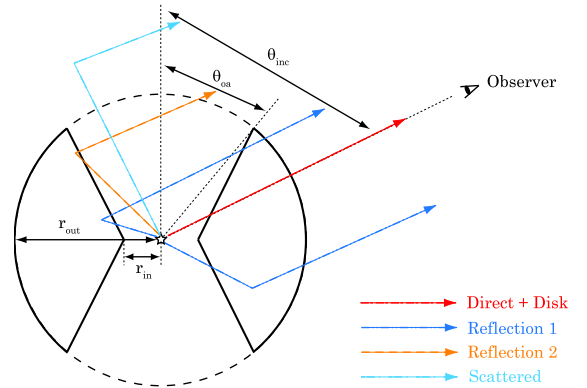

Figure 6. Cross-section view of the torus geometry assumed in Ikeda et al. (2009). The torus structure is characterized by the half-opening angle $\theta_{\rm oa}$, the inclination angle of torus from an observer $\theta_{\rm inc}$, the hydrogen column density viewed from the equatorial plane $N_{\rm H}^{\rm Eq}$, and the ratio of $r_{\rm in}$ to $r_{\rm out}$. The observed lights consist of a transmitted component absorbed by the torus (dash-dashed red), a reflection component from the accretion disk absorbed by the torus (dash-dashed red), two reflection components by the torus; "reflection component 1" absorbed by the torus (dash-dot-dotted blue) and "reflection component 2" not absorbed by it (dashed orange). We also consider a scattered component by the surrounding gas, which is not absorbed by the torus (dash-dash-dotted cyan).

sistent with the contraints from the *Swift*/BAT spectra for both targets (> 300 keV). Since the fit is performed only in the 0.5–100 keV range where the table model is available, the choice of $E_{\rm cut}$ hardly affects our results as far as it is higher than ~ 300 keV. We consider two cases for the elemental abundances; "Solar" abundances (as defined by Anders & Grevesse 1989) and "Subsolar" ones where only those of iron and nickel are set to be 0.5 times Solar values. Finally, the table files have five free parameters; $N_{\rm H}^{\rm Eq}$, $\theta_{\rm oa}$, $\theta_{\rm inc}$, the photon index Γ of the incident continuum, and its normalization at 1 keV.

In the assumed geometry of the torus, the line-of-sight hydrogen column density $N_{\rm H}$ for the transmitted component is related to that along the equatorial plane ($N_{\rm H}^{\rm Eq}$) via equation (3) in Ikeda et al. (2009):

$$\frac{N_{\rm H}}{N_{\rm H}^{\rm Eq}} = \frac{r\left(\cos\theta_{\rm inc} - \cos\theta_{\rm oa}\right) + \sin\left(\theta_{\rm inc} - \theta_{\rm oa}\right)}{(1-r)\left\{r\cos\theta_{\rm inc} + \sin\left(\theta_{\rm inc} - \theta_{\rm oa}\right)\right\}}. \quad (1)$$

We introduce **torusabs** (for the fixed Solar abundances) and **vtorusabs** models (for variable abundances) as local models of *XSPEC* to represent photoelectric absorption of the transmitted component, whose line-of-sight column density is related to the torus parameters according to the above equation. In these models we take into account Compton scattering processes in addition to photoelectric absorption, and hence they can be reliably used even for the Compton thick case. We adopt the photoelectric absorption cross section by Verner et al. (1996) for consistency with Ikeda et al. (2009). As noted by Ikeda et al. (2009), the cross section by Verner et al. (1996) is more accurate for energies above 10 keV than that by Balucinska-Church & McCammon (1992), and is nearly equal to the NIST XCOM database.[12] Since the results become physically meaningless for obscured AGNs if we obtain $\theta_{\rm inc} < \theta_{\rm oa}$, we impose the condition that $\theta_{\rm inc} \geq \theta_{\rm oa} + 1°$ in the fitting process.

The fraction of the scattered component to the transmitted component, $f_{\rm scat}$, should be proportional to the opening solid angle of the torus if the column density of the scattering gas is constant. Thus, we have the constraint that

$$\cos\theta_{\rm oa} = 1 - \frac{f_{\rm scat}}{f_{\rm scat,0}}\left(1 - \cos\theta_{\rm oa,0}\right), \quad (2)$$

where we normalize $f_{\rm scat} = f_{\rm scat,0}$ at $\theta_{\rm oa} = \theta_{\rm oa,0} \equiv 45°$. Similarly, we also developed the **fscat** model for *XSPEC* to calculate the normalization of the scattered emission as a function of two parameters, $\theta_{\rm oa}$ and $f_{\rm scat,0}$. Here the normalization parameter $f_{\rm scat,0}$ reflects the averaged column density of the scattering gas and is treated as a free parameter. We allow it to vary within 0.1%–5%; note that a typical value in Seyfert 2 galaxies is $f_{\rm scat} = 3\%$ (Guainazzi et al. 2005).

In addition to the reprocessed emission from the torus, we should also expect a reflection component from the accretion disk in AGN spectra. Thus, in the transmitted component, we include this effect by utilizing the **pexrav** model (Magdziarz & Zdziarski 1995), which is appropriate to represent the reflection component from semi-infinite plane, like that from accretion disks. Here we fix

the strength of the disk reflection to be $R \equiv \Omega/2\pi = 1$, where Ω is the solid angle of the accretion disk. The inclination angle of the accretion disk is linked to that of the torus. Although the contribution of this component is not included in the incident photon spectrum in the Ikeda et al. (2009) model, the effects on the "torus reflection" spectra are only second-order and are negligible. For simplicity, hereafter we refer to the total spectrum including the reflection component from the accretion disk as "torus model".

To summarize, we can write the torus model of the photon spectrum $F(E)$ without the Galactic absorption as follows:

$$F(E) =$$
$$\exp\left\{-N_{\rm H}\left(N_{\rm H}^{\rm Eq}, \theta_{\rm oa}, \theta_{\rm inc}\right)\sigma(E)\right\}I(E)$$
$$+ f_{\rm scat}\left(\theta_{\rm oa}, f_{\rm scat,0}\right)I(E)$$
$$+ \exp\left\{-N_{\rm H}\left(N_{\rm H}^{\rm Eq}, \theta_{\rm oa}, \theta_{\rm inc}\right)\sigma(E)\right\}R_{\rm disk}(\theta_{\rm inc}, E)$$
$$+ R_{\rm refl,1}\left(N_{\rm H}^{\rm Eq}, \theta_{\rm oa}, \theta_{\rm inc}\right)$$
$$+ R_{\rm refl,2}\left(N_{\rm H}^{\rm Eq}, \theta_{\rm oa}, \theta_{\rm inc}\right)$$
$$+ \varepsilon_{\rm Fe}L_{\rm Fe}\left(N_{\rm H}^{\rm Eq}, \theta_{\rm oa}, \theta_{\rm inc}\right)$$
$$+ S(E), \quad (3)$$

where $I(E) \equiv AE^{-\Gamma}\exp\left(-E/E_{\rm cut}\right)$ is the intrinsic cutoff power-law component, A is the normalization parameter of the intrinsic cutoff power law at 1 keV, $N_{\rm H}^{\rm Eq}$ is the hydrogen column density of the torus viewed from the equatorial plane, $\theta_{\rm oa}$ is the half-opening angle of the torus, $\theta_{\rm inc}$ is the inclination angle of the torus, $f_{\rm scat,0}$ is the normalization parameter at $\theta_{\rm oa} = 45°$, $N_{\rm H}\left(N_{\rm H}^{\rm Eq}, \theta_{\rm oa}, \theta_{\rm inc}\right)$ is the absorption column density for the transmitted component, $\sigma(E)$ is the cross section of photoelectric absorption, $f_{\rm scat}\left(\theta_{\rm oa}, f_{\rm scat,0}\right)$ is the scattered fraction, $R_{\rm disk}(\theta_{\rm inc}, E)$ is the Compton reflection component from the accretion disk, $R_{\rm refl,1}\left(N_{\rm H}^{\rm Eq}, \theta_{\rm oa}, \theta_{\rm inc}\right)$ is the torus-reflection component 1 (see Figure 6), $R_{\rm refl,2}\left(N_{\rm H}^{\rm Eq}, \theta_{\rm oa}, \theta_{\rm inc}\right)$ is the torus-reflection component 2 (see Figure 6), $\varepsilon_{\rm Fe}$ is the normalization parameter for the iron-K emission line, $L_{\rm Fe}\left(N_{\rm H}^{\rm Eq}, \theta_{\rm oa}, \theta_{\rm inc}\right)$ is the iron-K emission line, and $S(E)$ represents additional soft components (for the case of NGC 3081 where the **apec** model is used). We allow the relative normalization of the iron-K line $\varepsilon_{\rm Fe}$ with respect to the torus-reflection components to float between 0.5 and 2, in order to cover the iron abundance range over the fixed values (0.5 or 1.0) and to model the effects of time variability between the transmitted component and the averaged reprocessed emission.

In short, Equation (3) is expressed as absorbed transmission[13] + scattering[14] + absorbed accretion disk re-

---

[12] http://www.nist.gov/pml/data/xcom/index.cfm

[13] In *XSPEC* nomenclature, **torusabs*zhighect*zpowerlw**
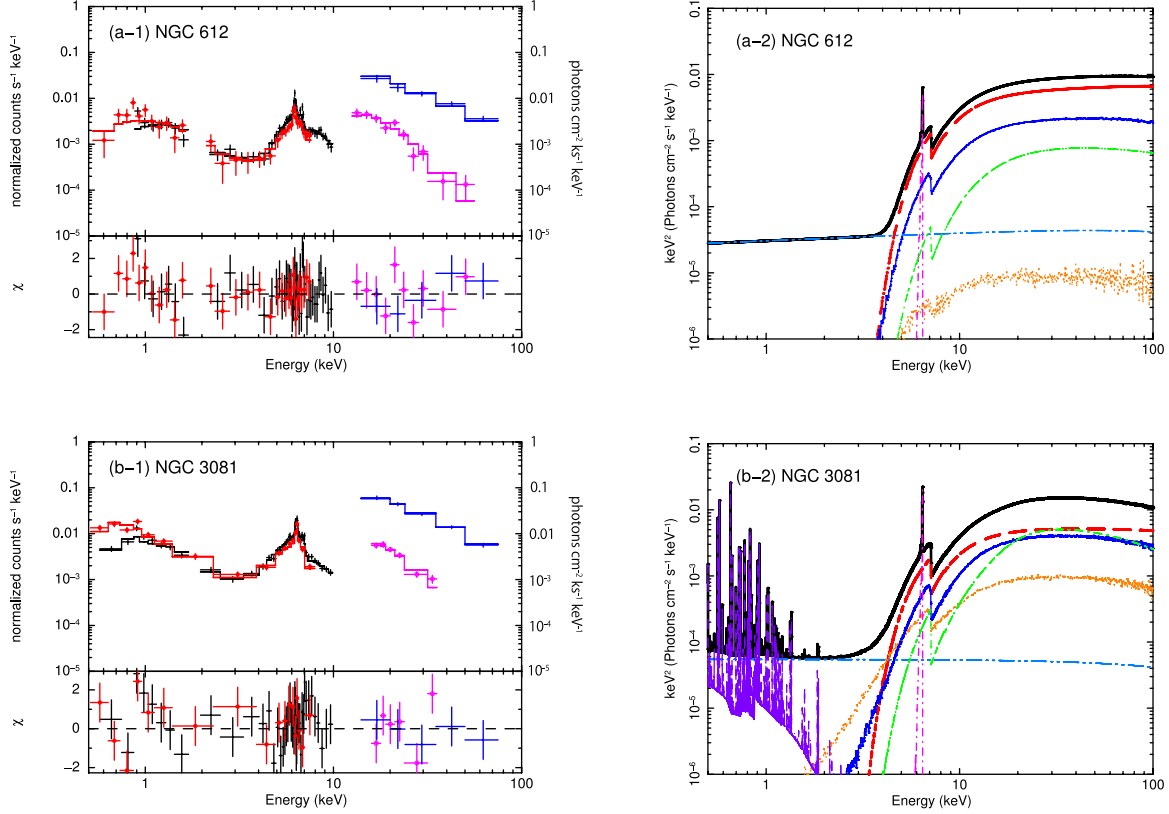[14] In *XSPEC* nomenclature, **fscat*zhighect*zpowerlw**

Figure 7. The observed spectra (left) and the best-fit spectral model (right) with the torus model. *Left*: same as Figure 4 (left). *Right*: the best-fit spectral model in units of EF_E (where E is the energy and F_E is the photon spectrum); total (thick black), transmitted component (thick dashed red), reflection component from the accretion disk (thin dot-dashed green), torus reflection component 1 (thin blue), torus reflection component 2 (thin dotted orange), scattered component (thin dot-dot-dashed cyan), iron-K emission line (thin dot-dashed magenta). The purple dashed curve below 2 keV in NGC 3081 represents the emission from an optically-thin thermal plasma.

flection[15] + absorbed torus reflection[16] + unabsorbed torus reflection[17] + iron line[18]. There are eight free parameters: $\theta_{\rm inc}$, $\theta_{\rm oa}$, $N_{\rm H}^{\rm Eq}$, $f_{\rm scat,0}$, $E_{\rm cen}$, $\varepsilon_{\rm Fe}$, A, and Γ. In the spectral fit, we employ the *MINUIT MIGRAD* method ("migrad") as the fitting algorithm, which is found to be more stable than the standard *Levennerg-Marquardt* method ("leven") in our case utilizing the numerical models. Both of the *Suzaku* and BAT spectra (but below 100 keV) are used throughout this section.

4.2. Application

4.2.1. NGC 612

Figure 7 plots the best-fit torus model, whose parameters are summarized in Table 5. The torus model with "Subsolar" abundances is adopted for this target, based on the fitting result with the analytical models (Section 3). We find that $\theta_{\rm oa} \simeq 60° - 70°$ and $\theta_{\rm inc} \gtrsim 76°$. As shown in Figure 7, the contribution from the reflection component 2 (unabsorbed one) is very small, suggesting that we are seeing the target from an edge-on angle. In such case, the inclination angle $\theta_{\rm inc}$ can be poorly determined above a certain threshold, because the observed line-of-sight hydrogen column density is rather insensitive to $\theta_{\rm inc}$ for a given $N_{\rm H}^{\rm Eq}$ value. Actually, we

---

[15] In *XSPEC* nomenclature, **torusabs*toruspexrav**
[16] In *XSPEC* nomenclature, **atable{refl1_torus.fits}**
[17] In *XSPEC* nomenclature, **atable{refl2_torus.fits}**
[18] In *XSPEC* nomenclature, **constant*atable{refl_fe_torus.fits}**

find that the column density in the equatorial plane, $N_{\rm H}^{\rm Eq} \simeq 10^{24.1}$ cm^{-2}, is close to that along the line of sight ($N_{\rm H}$) as estimated from the analytical model fit. We also find that $f_{\rm scat,0} \simeq 0.14\%$, which indicates that the amount of scattering gas around the nucleus is remarkably small.

4.2.2. NGC 3081

The best-fit parameters with the torus model for NGC 3081 are summarized in Table 5 and the model is plotted in Figure 7. For this target, we adopt the "Solar" abundance tables based on the analytical model fit. We obtain $\theta_{\rm oa} \simeq 15°$, $\theta_{\rm inc} \simeq 19°$, $N_{\rm H}^{\rm Eq} \simeq 10^{24.0}$ cm^{-2}, and $f_{\rm scat,0} \simeq 4.6\%$. By contrast to NGC 612, $f_{\rm scat,0}$ is rather large, and there is a significant contribution from the unabsorbed reflection component, indicating that the inclination angle must be close to the torus opening angle. The results are consistent with the picture proposed for the "new type" AGN SWIFT J0601.9–8636 (ESO 005–G004) by Ueda et al. (2007), that the nucleus is deeply buried in the geometrically thick torus and is observed from a rather face-on angle.

5. DISCUSSION AND CONCLUSION

With *Suzaku* follow-up, we have obtained the best-quality broad band spectra covering the 0.5–60 keV band of two *Swift*/BAT AGNs, NGC 612 and NGC 3081. First, we found a range in the iron abundance; NGC 612 has about 0.5 times Solar abundance of iron (where "So-

Table 5
Best-fit Spectral Parameters with Torus Model

		NGC 612	NGC 3081
(1)	Table model	Subsolar	Solar + apec[a]
(2)	$N_{\rm H}^{\rm Gal}$ (10^{22} cm^{-2})	0.0195	0.0388
(3)	$N_{\rm H}^{\rm Eq}$ (10^{22} cm^{-2})	113^{+10}_{-8}	91^{+10}_{-9}
(4)	$\theta_{\rm oa}$[b] (degrees)	70 (> 58)	15 ± 2
(5)	$\theta_{\rm inc}$ (degrees)	87 (> 76)	19^{+7}_{-1}
(6)	Γ	1.9 ± 0.1	2.0 ± 0.1
(7)	$f_{\rm scat,0}$ (%)	0.14 (< 0.19)	4.6 (> 3.1)
(8)	$E_{\rm cen}$ (keV)	$6.43^{+0.11}_{-0.02}$	$6.42^{+0.03}_{-0.04}$
(9)	$\varepsilon_{\rm Fe}$	$1.6^{+0.4}_{-0.6}$	0.57 (< 0.69)
	χ^2/d.o.f.	84.3/83	209.0/200

Note. — (1) The table model used in the fit. "Solar" means the table with Solar abundances, while "Subsolar" means the table with 0.5-time iron and nickel abundances with respect to Solar ones. (2) The hydrogen column density of Galactic absorption by Kalberla et al. (2005). (3) The hydrogen column density of the torus viewed from the equatorial direction. (4) The half opening angle of the torus. (5) The inclination angle of the torus. (6) The power-law photon index. (7) The fraction of the scattered component relative to the intrinsic power law when the half opening angle of the torus is 45°. (8) The center energy of the iron-K emission line at the rest frame of the source redshift. (9) The relative strength of the iron-K emission line to that predicted by the torus model. The errors are 90% confidence limits for a single parameter.

[a] An additional emission from an optically-thin thermal plasma with Solar abundances is required, modelled by the **apec** code with a temperature of $kT = 0.25 \pm 0.02$ keV and an emission measure of 1.5×10^{63} cm^{-3} (see text).

[b] The range of the $\theta_{\rm oa}$ is limited to $< 70°$ in the torus model.

lar" corresponds to Fe/H = 4.68×10^{-5}), which is significantly smaller than that of NGC 3081. Applying the analytical models, we find that these objects are nearly Compton thick AGNs with $N_{\rm H} \simeq 10^{24}$ cm^{-2} and the fraction of the scattered component with respect to the transmitted component is small, $f_{\rm scat} < 0.8\%$, suggesting that these belong to "hidden" population according to Winter et al. (2009). Plotting the results in the $f_{\rm scat}$ versus reflection strength (R) plane, we find these two targets are located just between those occupied by "new type" (geometrically thick tori) and "classical type" AGNs defined in Paper I, implying that they would be an intermediate class bridging the two types. We need a larger sample to reveal the true distribution of the whole AGN population in this plane. In this context, simultaneous broad band observations of more "new type" candidates are important to examine their reflection strengths, such as those with small scattering fractions identified from the *XMM-Newton* catalog (Noguchi et al. 2009).

To further investigate the details of the torus geometry of the two AGNs, we apply numerical spectral models based on Monte Carlo simulation where a simple 3-dimensional geometry of the torus is assumed, following the work by Ikeda et al. (2009) and Awaki et al. (2009). We also consider the Compton reflection component from the accretion disk. To our knowledge, this is the first time all effects both from the torus and disk are self-consistently considered in spectral analysis of obscured AGNs. It is remarkable that we are able to reproduce the observed spectra quite well with this torus model, which has only 3 free geometrical parameters; the opening angle, inclination, and equatorial column density.

The column density along the equator plane is found to be $N_{\rm H} \approx 10^{24}$ cm^{-2} for both sources, which is also similar to that found from the Seyfert 2 galaxy Mrk 3 by Ikeda et al. (2009). The relative absence of higher column densities, though very limited in number, may be consistent with the fact that even hard X-rays above 10 keV have a bias against detecting heavily Compton thick AGNs with $N_{\rm H} \sim 10^{25}$ cm^{-2}, unless the sample is limited to the very local universe (Malizia et al. 2009). Thus, a majority of *Swift*/BAT AGNs do not have extremely Compton thick tori defined at the equator plane unless observed from a face-on angle. Future sensitive hard X-ray surveys may start to pick up such populations, whose number density and cosmological evolution are still open questions.

The analysis with the torus model suggest that the torus geometry of the two targets may be different in spite of the very similar results obtained from the analytical models. Our results confirm that the fundamental assumption of the unified model where the opening angles are all the same is too simple. For NGC 612, we find that the opening angle is relatively large ($\simeq 60° - 70°$) and the object is observed from an edge-on angle, consistent with a picture of "classical type" Seyfert 2 galaxies. Similar torus parameters are obtained for Mrk 3 by Ikeda et al. (2009). By contrast, the torus opening angle of NGC 3081 is much smaller ($\simeq 15°$), and we observe it from a face-on angle. This implies that NGC 3081 is closer to a "new type" AGN discovered by Ueda et al. (2007) surrounded by a geometrically thick torus. This picture for NGC 3081 is consistent with the time variability of the column density, because we are seeing the thinnest part of the torus that is expected to be highly patchy (Risaliti et al. 2002). We note, however, that the best-fit torus parameters we obtain from the present analysis should not be taken at their face values, which could depend on the initial assumption of the torus geometry. For instance, as discussed in Ikeda et al. (2009), if we assume a lower value for $r (\equiv r_{\rm in}/r_{\rm out})$ than 0.01, we would obtain a slightly larger half-opening angle $\theta_{\rm oa}$ for the same $N_{\rm H}^{\rm Eq}$ and $\theta_{\rm inc}$ to account for the increased contribution of the unabsorbed reflection component.

Since the observed scattering fraction is similar between the two targets, this difference in the torus opening angle indicates that the amount of scattering gas around the nucleus is much smaller in NGC 621 than in NGC 3081, as represented in the obtained $f_{\rm scat,0}$ value, $f_{\rm scat,0} < 0.2\%$ for NGC 612 and $f_{\rm scat,0} > 3\%$ for NGC 3081. The small amount of the gas in NGC 612 may be consistent with its classification as a "weak emission line" radio galaxy, where the jets expel the surrounding gas. By contrast, the detection of the optically-thin components in NGC 3081 could represent the abundance of the ambient gas around the nucleus.

An important implication from the present study is that the classification of different types of tori (e.g., geometrically thin or thick) based solely on the scattered fraction may be difficult in some cases. Our work has demonstrated the power of the application of numerical torus models based on Monte Carlo simulation to best extract the physical view of the nucleus beyond the simple phenomenological spectral analysis, although caution must be paid because we have considered only the sim-

plest geometry by assuming a uniform density. Combinations of the high quality broad band X-ray spectra with more realistic numerical simulations will be a key approach for further understanding of the nature of AGNs.

REFERENCES

Anders, E., & Grevesse, N. 1989, Geochim. Cosmochim. Acta, 53, 197
Awaki, H., Terashima, Y., Higaki, Y., & Fukazawa, Y. 2009, PASJ, 61, 317
Balucinska-Church, M. & McCammon, D. 1992, ApJ, 400, 699
Bassani, L., et al. 2006, ApJ, 636, L65
Comastri, A., Iwasawa, K., Gilli, R., Vignali, C., & Ranalli, P. 2009, arXiv:0910.1025
Comastri, A., Iwasawa, K., Gilli, R., Vignali, C., Ranalli, P., Matt, G., & Fiore, F. 2010, ApJ, 717, 787
Dotani, T. & the XIS team 2007, JX-ISAS-SUZAKU-MEMO-2007-08
Eguchi, S., Ueda, Y., Terashima, Y., Mushotzky, R., & Tueller, J. 2009, ApJ, 696, 1657
Fanaroff, B. L., & Riley, J. M. 1974, MNRAS, 167, 31P
Freeman, T., Byrd, G., & Ousley, D. 2000, IAU Colloq. 174: Small Galaxy Groups, 209, 325
Gilli, R., Comastri, A., & Hasinger, G. 2007, A&A, 463, 79
Gopal-Krishna, & Wiita, P. J. 2000, A&A, 363, 507
Guainazzi, M., Matt, G., & Perola, G. C. 2005, A&A, 444, 119
Hopkins, P. F., Hernquist, L., Cox, T. J., Di Matteo, T., Martini, P., Robertson, B., & Springel, V. 2005, ApJ, 630, 705
Ikeda, S., Awaki, H., & Terashima, Y. 2009, ApJ, 692, 608
Joshi, U. C., Jain, R., & Deshpande, M. R. 1989, Active Galactic Nuclei, 134, 321

Kalberla, P. M. W., Burton, W. B., Hartmann, D., Arnal, E. M., Bajaja, E., Morras, R., Pöppel, W. G. L. 2005, A&A, 440, 775
Krivonos, R., Revnivtsev, M., Lutovinov, A., Sazonov, S., Churazov, E., & Sunyaev, R. 2007, A&A, 475, 775
Maeda, Y., Someya, K., Ishida, M., & the XRT team, Hayashida, K., Mori, H., & the XIS team 2008, JX-ISAS-SUZAKU-MEMO-2008-06
Magdziarz, P., & Zdziarski, A. A. 1995, MNRAS, 273, 837
Magorrian, J., et al. 1998, AJ, 115, 2285
Malizia, A., Stephen, J. B., Bassani, L., Bird, A. J., Panessa, F., & Ubertini, P. 2009, MNRAS, 399, 944
Marconi, A., & Hunt, L. K. 2003, ApJ, 589, L21
Matt, G., Perola, G. C., & Piro, L. 1991, A&A, 247, 25
Mitsuda, K., et al. 2007, PASJ, 59, 1
Mizuno, T., et al. 2008, JX-ISAS-SUZAKU-MEMO-2008-03
Moran, E. C., Kay, L. E., Davis, M., Filippenko, A. V., & Barth, A. J. 2001, ApJ, 556, L75
Morganti, R., Killeen, N. E. B., & Tadhunter, C. N. 1993, MNRAS, 263, 1023
Murphy, K. D., & Yaqoob, T. 2009, MNRAS, 397, 1549
Nakajima, H., et al. 2008, PASJ, 60, 1
Nandra, K., & Pounds, K. A. 1994, MNRAS, 268, 405
Noguchi, K., Terashima, Y., & Awaki, H. 2009, ApJ, 705, 454
Ozawa, M., et al. 2009, PASJ, 61, 1
Parisi, P., et al. 2009, A&A, 507, 1345
Risaliti, G., Elvis, M., & Nicastro, F. 2002, ApJ, 571, 234
Storchi-Bergmann, T., Kinney, A. L., & Challis, P. 1995, ApJS, 98, 103
Tueller, J., Mushotzky, R. F., Barthelmy, S., Cannizzo, J. K., Gehrels, N., Markwardt, C. B., Skinner, G. K., & Winter, L. M. 2008, ApJ, 681, 113
Ueda, Y., Akiyama, M., Ohta, K., & Miyaji, T. 2003, ApJ, 598, 886
Ueda, Y., et al. 2007, ApJ, 664, L79
Verner, D. A., Ferland, G. J., Korista, K. T., & Yakovlev, D. G. 1996, ApJ, 465, 487
Winter, L. M., Mushotzky, R. F., Tueller, J., & Markwardt, C. 2008, ApJ, 674, 686
Winter, L. M., Mushotzky, R. F., Reynolds, C. S., & Tueller, J. 2009, ApJ, 690, 1322